Aeroelastic Stability of Composite Hingeless Rotor Blades in Hover—Part II: Results

M. V. FULTON* AND D. H. HODGES
School of Aerospace Engineering, Georgia Institute of Technology
Atlanta, GA, U.S.A.

Abstract—In Part I of this two-part paper, an aeroelastic stability analysis was presented for isolated hingeless, composite rotor blades in the hovering flight condition, which was based on a mixed finite element method. Herein, the focus is to present numerical results obtained from this analysis. First, certain of these results are compared with those of existing aeroelastic stability analyses for validation. Next, the numerical accuracy and convergence characteristics of the current approach are quantified. Finally, parametric studies are performed to investigate the effects of composite elastic coupling and thrust condition on the blade's aeroelastic stability, especially that of the lightly damped lead-lag mode. The stability of some of the elastically coupled cases studied was sensitive to the nonclassical couplings; indeed, in one case a significant error appeared, accentuated at high thrust levels, when bending-shear coupling was neglected. Another significant effect stems from changes in the equilibrium solution for elastic twist due to extension-twist coupling. The necessity of including such effects in the blade model for general-purpose analysis is noted.

1. INTRODUCTION

In this paper, which is Part II of a two-part paper, we present and discuss certain numerical results obtained from the analysis developed in Part I. Our focus is on the validation of this analysis, examination of its accuracy and convergence properties, and generation of numerical results in order to study the aeroelastic stability of certain types of elastically coupled hingeless rotor blades.

Older works successfully exploited the use of spring-restrained, rigid-blade models, which permitted the efficient calculation of stability trends. For instance, the effects of precone, aerodynamic modeling, flap-lag, pitch-lag, and pitch-flap couplings on stability were investigated. Interestingly enough, it was shown that flap-lag elastic couplings, along with pitch-lag and pitch-flap kinematic couplings, noticeably affected stability. Positive precone, for instance, was shown to affect the equilibrium position, thereby modifying the pitch-lag and pitch-flap couplings and adversely affecting stability (but reducing equilibrium bending moments as desired) [1].

Little work has been done to verify that similar trends can be obtained for couplings which arise from laminate design rather than root hinge orientation. Rather, the specifics of the trends, along with the significance of composite modeling parameters, are still being investigated. In this section, previous results are reviewed, existing analytical capabilities are compared with the

---

Typeset by $\mathcal{A}_{\mathcal{M}}\mathcal{S}$-TEX

current analysis, and the current work is introduced.

One of the most recent composite stability analyses is that of [2]. Unlike [3], which documented no validation for non-isotropic configurations, [2] performed significant validation studies for orthotropic configurations. For instance, [2] compared *in vacuo* results for the rotating natural frequencies of extension-twist and bending-twist coupled composite box beams with the experimental results of [4] and analytical results based upon the three-dimensional analysis of [5]. These correlations showed that the analysis of [2] generally predicted the first and second flap, first and second lead-lag, and first torsion rotating frequencies within five to ten percent of the experimental results. Although the analysis of [5] generally predicted frequencies better than [2], there were a few cases for which the opposite was true. Stability results for a configuration similar to the BO-105 hingeless rotor were calculated. The baseline configuration was a 26-ply box beam with no material couplings; the coupled cases were typically obtained by modifying the baseline configuration through the re-orientation of three of the plies. This small modification allowed the introduction of couplings without significantly altering the rotating natural frequencies of the rotor blades. Three "symmetric" cases (two pitch-flap and one pitch-lag) and one "antisymmetric" case (extension-twist) were studied. As in [3], [2] demonstrated that a change in the material couplings can significantly modify the damping of the lead-lag mode.

Another recent work was that of [6]. Although principally an investigation of tip sweep and anhedral effects, [6] compared their results to one bending-twist case from [3]. [6] predicted trends which are qualitatively similar to [3] while being quite different quantitatively. This comparison is the only validation study reported in [6].

Overall, the capabilities of the current analysis are rather similar to the analyses of [2,6]. All three analyses include shear deformation and model geometrically nonlinear effects. The present analysis, however, does not invoke a moderate deflection assumption. Unlike the present analysis and [2], [6] includes restrained, out-of-plane, torsional warping effects and uses the uniaxial stress assumption. The most obvious distinction between the current work and those of [2,6] is that the current analysis is based on a mixed variational formulation [7]. This new formulation gives the advantages of having a very sparse Jacobian, of permitting the use of simple shape functions, and of calculating the strains and stresses as accurately as the displacements. In addition, the formulation facilitates the derivation of the terms of the Jacobian and the residual in closed form. The equations have an orderly structure and can be written exactly in a few lines (as opposed to several pages of equivalent equations for a moderate-deflection-based formulation).

This new formulation has been implemented in a FORTRAN program named STAB. STAB has been validated against analytical, numerical, and experimental results for linear and nonlinear static and dynamic calculations for nonrotating beams [8–11]. This paper has three main sections: (1) physical characteristics of models, (2) aeroelastic stability validation studies, and (3) parametric studies.

2. PHYSICAL CHARACTERISTICS OF MODELS

In later sections, results are given for various rotor configurations. Each configuration, or model, has certain basic characteristics such as length, distributed mass, and operational parameters such as rotor speed and number of blades. Since multiple sets of results have been obtained for some of the models, all physical characteristics for these models are presented in this section. The blades for all rotor configurations were spanwise uniform and initially straight and untwisted; all rotors were assumed to have identical blades with the airfoil's zero-lift-line coincident with b_2, the undeformed coordinate axis, which is horizontal when there is no precone. Each blade's reference coordinate system was aligned with the principal axes. Finally, in all models, the blade weight was neglected.

2.1. Hypothetical Rotor

The Hypothetical Rotor described in [12] was an isolated, hingeless rotor with blades which had no material couplings. The properties of this rotor are given in Table 1. (See Table 3 for a description of the variables.)

Table 1. Rotor characteristics for rotors hypothetical, HC, and R2.

Variable	Rotor		
	Hypothetical	HC	R2
e	0.0	0.0	0.0
ℓ (in)	36.0	254.6	35.23
c (in)	3.5	20.0	2.6
ρ (lb-s^2/in^2)	4.313×10^{-5}	0.001996	3.18×10^{-5}
I_{11} (lb-s^2)	4.313×10^{-5}	2.8×10^{-2}	2.26×10^{-5}
ω_{a3} (RPM)	1000	250	2077
ρ_∞ (lb-s^2/in^4)	1.146×10^{-7}	1.146×10^{-7}	1.146×10^{-7}
a	6.28	5.7	6.283
c_{d_o}	0.01	0.01	0.0079
b	2.0	4.0	2.0

2.2. Rotor HC

Aeroelastic stability results were generated for four rotors with blades modeled as box beams and studied in [3]. For these rotors, the configuration detailed in Table 1 was used. The rotor speed and the polar mass moment of inertia were chosen to match the *in vacuo* rotating natural frequencies given in [3] as closely as possible. These properties yielded flap, lag, and torsion frequencies, nondimensionalized by the rotor speed, of $\omega_w = 1.17$, $\omega_v = 1.45$, and $\omega_\phi = 5.06$ (as compared to $\omega_w = 1.15$, $\omega_v = 1.5$, and $\omega_\phi = 5.0$ from [3]). Each blade had a thin-walled box beam as its principal structural element, with the graphite-epoxy material properties given in Table 2. The four configurations include two cases which exhibit bending-twist coupling and two which exhibit extension-shear coupling. In each case, two opposing sides of the box have all zero degree plies, with the other two sides containing some angle plies. Case I has the angle plies on the inner half of the sides to create pitch-lag coupling, and Case II has angle plies on the inner half of the top and bottom to create pitch-flap coupling. Case III has plies on the inner one-eighth of the sides, and Case IV has plies on the inner one-eighth of the top and bottom. (Cases I and II are referred to as "symmetric" cases by [3]; III and IV are called "antisymmetric.") The cross-sectional properties (see Tables 4 and 5) were calculated using ATWCS; TAIL was used to generate the nonlinear torsional stiffness coefficient (which was not available from ATWCS).

Table 2. Material properties for the graphite-epoxy used for box HC and for the graphite-epoxy AS4/3501-6.

Variable	Box HC	AS4/3501-6
E_{11}	30.0×10^6 psi	142.0 GPa
E_{ss}	3.0×10^6 psi	9.81 GPa
G_{1s}	1.2×10^6 psi	6.0 GPa
G_{23}	0.97×10^6 psi	3.77 GPa
ν_{1s}	0.3	0.3
ν_{23}	0.34	0.34
t_{ply}	0.04375 in	0.000134 m

Table 3. Rotor R1 characteristics.

Variable	Description	Rotor R1
e	root offset	0.0
ℓ (m)	rotor length	0.9615
c (m)	chord	0.0864
ρ (kg/m)	rotor mass/length	0.343
I_{11} (kg m)	blade polar mass moment of inertia/length	2.062×10^{-4}
ω_{a3} (RPM)	rotor speed	1000.0
ρ_∞ (kg/m^3)	air density	1.225
a	lift-curve slope	6.283
c_{d_o}	coefficient of drag	0.0079
b	number of blades	2.0

Table 4. ATWCS stiffnesses for box HC, Cases I and II.

Stiffness	$\zeta = 0°$	I,$\zeta = 30°$	II, $\zeta = 20°$
A_{11}, lb	0.1743×10^9	0.1608×10^9	0.1320×10^9
D_{11}, lb-in^2	0.1218×10^8	0.1388×10^8	0.2081×10^8
D_{12}, lb-in^2	—	—	-0.1442×10^8
D_{13}, lb-in^2	—	0.6860×10^7	—
D_{22}, lb-in^2	0.1029×10^9	0.9986×10^8	0.8411×10^8
D_{33}, lb-in^2	0.8977×10^9	0.7524×10^9	0.7418×10^9

Table 5. ATWCS stiffnesses for box HC, Cases III and IV.

Stiffness	III, $\zeta = 30°$	IV, $\zeta = 30°$
A_{11}, lb	0.1716×10^9	0.1647×10^9
B_{11}, lb-in	0.1013×10^7	0.5170×10^7
D_{11}, lb-in^2	0.1303×10^8	0.1650×10^8
D_{22}, lb-in^2	0.1023×10^9	0.9530×10^8
D_{33}, lb-in^2	0.8670×10^9	0.8565×10^9

2.3. Rotor R2

R2 is based upon the rotor given in [13]. Certain assumptions had to be made, however, to come up with a complete set of rotor properties. Specifically, the area centroidal axis for the structural portion of each blade was taken to be located at the quarter chord of the NACA 0012 airfoil and was assumed to be coincident with the blade's mass centroidal axis. The polar mass moment of inertia was assumed, along with the number of blades. In addition, the root offset was set to zero, with the rotor radius taken to equal that of [13]. The details of this soft in-plane configuration can be found in Table 1. The cross-sectional properties were taken directly from [13].

2.4. Rotor R1

R1 is based upon [14] and has the properties given in Table 3. The material chosen for this rotor was AS4/3501-6 (see Table 2). As with R2, certain assumptions had to be made to come up with a complete set of rotor properties. Specifically, the area centroidal axis for the structural portion of each blade was taken to be located at the quarter chord of the NACA 0012 airfoil and was assumed to be coincident with the blade's mass centroidal axis. R1 was taken to have a box beam as the principal structural element. The horizontal and vertical dimensions of the midplane of the laminate were 0.0120 m and 0.00814 m, respectively. Two

laminates (L2e and L3e), were investigated, both being circumferentially uniform, fitting within the airfoil contour, and producing soft in-plane rotors. L2e had a lay-up of $[0_2/\zeta_4]$, and L3e was the $[\zeta, \zeta - 90, \zeta, (\zeta - 90)_2, \zeta]$ laminate studied in [13]. These two laminates have fundamental frequencies which are not strongly dependent upon the ply angle ζ. In general, the cross-sectional properties (see Tables 6 and 7) were calculated using ATWCS (which generates a 4 × 4 stiffness matrix); TAIL was used to generate the nonlinear torsional stiffness coefficient and to provide a 6 × 6 stiffness matrix to study the effects that different stiffness matrices have on stability.

Table 6. ATWCS stiffnesses for rotor R1 L2e.

Stiffness	$\zeta = 0°$	$\zeta = 20°$	$\zeta = 90°$
A_{11}, N	0.4599×10^7	0.3659×10^7	0.1753×10^7
B_{11}, N-m	—	0.3187×10^4	—
D_{11}, N-m^2	0.4571×10^1	0.9891×10^1	0.4571×10^1
D_{22}, N-m^2	0.5565×10^2	0.3185×10^2	0.2121×10^2
D_{33}, N-m^2	0.9979×10^2	0.5712×10^2	0.3803×10^2

Table 7. ATWCS stiffnesses for rotor R1 L3e.

Stiffness	$\zeta = 0°$	$\zeta = -20°$
A_{11}, N	0.2470×10^7	0.1938×10^7
B_{11}, N-m	—	-0.2959×10^4
D_{11}, N-m^2	0.4571×10^1	0.1150×10^2
D_{22}, N-m^2	0.2989×10^2	0.1424×10^2
D_{33}, N-m^2	0.5360×10^2	0.2554×10^2

3. AEROELASTIC STABILITY VALIDATION STUDIES

In this section, some of the studies which were performed to validate the theory and the associated computer program are described. Previous validation studies can be found in [8–11]. The validation studies described below were divided into three sections: (1) Convergence Study, (2) Stability Results, and (3) Numerical Issues.

3.1. Convergence Study

Two plots are included to quantify the accuracy of the finite element discretization of the governing equations. Both are for configuration R1 L3e ($[\zeta, \zeta - 90, \zeta, (\zeta - 90)_2, \zeta]$) with $\zeta = 0°$. Figure 1 shows the logarithm of the absolute value of the relative error of the equilibrium value of u_3 (flap-wise deflection) at the tip for a root pitch angle of 12°. Figure 2 shows the logarithm of the absolute value of the relative error of the lead-lag damping for a root pitch angle of 1°. Both quantities are shown versus the logarithm of the number of elements; each uses the solution for $N = 32$ elements to approximate the "exact" solution. Both figures indicate that the convergence is quite satisfactory: the relative error varied inversely with N^3 for the flapwise deflection case and inversely with N^6 for the lead-lag modal damping case. Figure 2 shows an error for $N = 16$ of approximately 0.003% for the lead-lag damping. All results, unless otherwise noted, were therefore generated using $N = 16$ elements.

The convergence rate for this finite element stability analysis was shown to be very good. Specifically, the relative error varied inversely with N^3 for the flapwise deflection of a high-thrust case (where N is the number of elements); the relative error varied inversely with N^6 for the lead-lag modal damping of a low-thrust case.
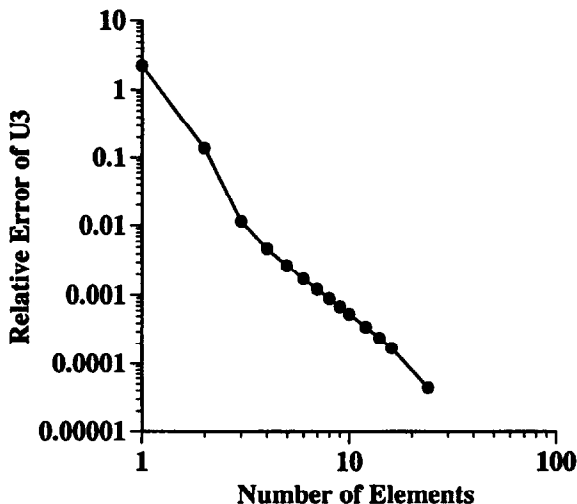
Figure 1. Absolute value of the relative error of the equilibrium value of u_3 (flapwise deflection) at the tip versus number of elements for R1 L3e ($[\zeta, \zeta - 90, \zeta, (\zeta - 90)_2, \zeta]$) with $\zeta = 0°$ and a root pitch angle of $12°$.
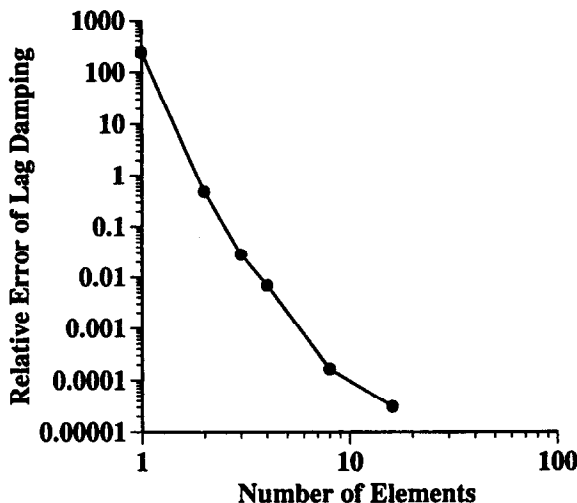

Figure 2. Absolute value of the relative error of the lead-lag damping versus number of elements for R1 L3e ($[\zeta, \zeta - 90, \zeta, (\zeta - 90)_2, \zeta]$) with $\zeta = 0°$ and a root pitch angle of $1°$.

3.2. Stability Results

To validate the stability results for the current code (STAB), results for the Hypothetical Rotor case [12] are compared to results generated by a previously validated stability code, PFLT [15]. Although PFLT used an ordering scheme to approximate the equilibrium solution, PFLT is sufficiently accurate to help validate the current computer code for moderate deflection results. In addition, results for Rotor HC are compared with results given in [3,6].

Figures 3 and 4 show the comparison of STAB results with those of PFLT for the Hypothetical Rotor. Figures 3 and 4 also give the damping and frequency versus pitch angle of the first lag mode for zero precone. Examination of these two figures, as well as similar figures for flap and torsion [11], indicates that STAB agrees quite well with PFLT for these cases. For these cases, agreement between STAB and PFLT is very good except for the torsion, which still has a relatively good correlation. In general, the results are best for small pitch angles, becoming worse as the pitch angle is increased. This tendency suggests that STAB does a better job of calculating the larger deflections than does PFLT, since the validity of deflections STAB can treat is not limited by the use of an ordering scheme. The additional torsional discrepancy occurs because

PFLT contains torsional modeling deficiencies (due to the ordering scheme) which cause it to do a worse job of predicting torsional behavior than the flap and lag motions. Cases with initial precone show larger variations between the two codes than found for the previous cases, but the agreement is still quite good (see [11]).
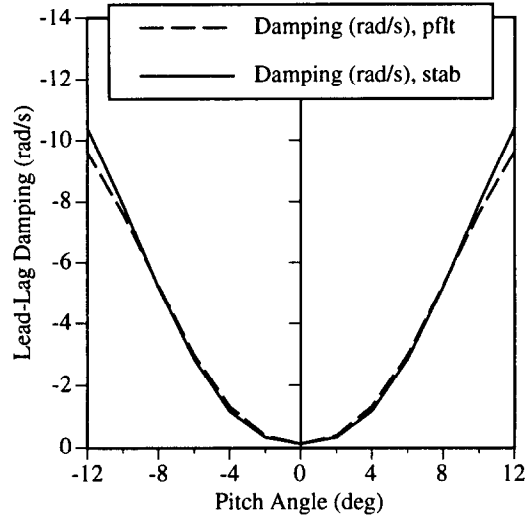

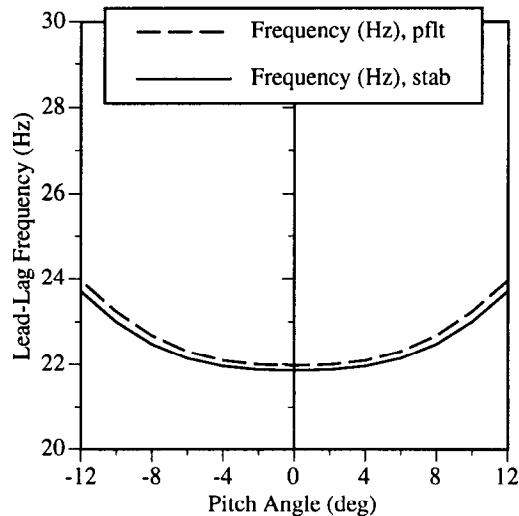Figure 3. Hypothetical rotor correlation, $\beta_{pc} = 0°$.

Figure 4. Hypothetical rotor correlation, $\beta_{pc} = 0°$.

Figures 5–8 show the lag damping for Cases I–IV of Rotor HC. The sign convention is such that $\zeta > 0$ creates $D_{13} > 0$ for Case I and $D_{12} < 0$ for Case II. $\zeta > 0$ creates a nose-down torsional deflection in response to a tensile load for Cases III and IV. Note that although [3] plotted its results as a function of ply angle, Figures 5–8 are plotted versus nondimensional lift. Results from [3] are included for C_T/σ, the coefficient of thrust/rotor solidity, equal to 0.1 for the three-ply angles in Figures 5 and 7 and two-ply angles in Figures 6 and 8. Results from [6] are also included for $C_T/\sigma = 0.05$ and 0.1 for the three-ply angles in Figure 5.

Two initial observations should be made. First, the large variation in the lag damping shown in Figure 6 for $\zeta = 20°$ is due to a strong coupling between the lag and flap modes. This coupling is enhanced because these two frequencies are very close to one another for this configuration. Second, there is only a small variation in results with ply angle for Cases III and IV.
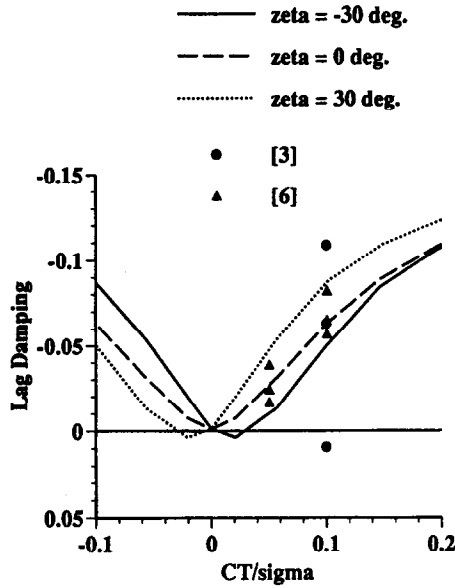
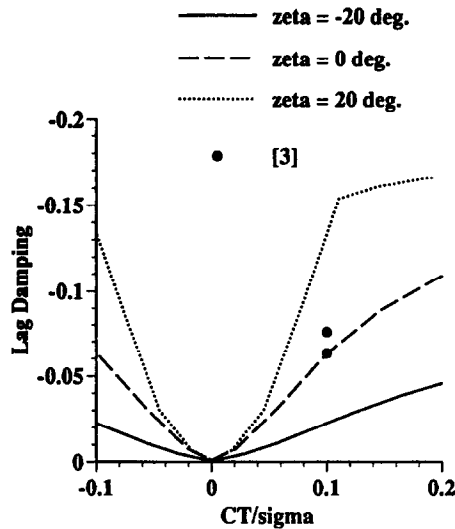Figure 5. Lag damping for box HC I (pitch-lag coupling).

Figure 6. Lag damping for box HC II (pitch-flap coupling).

Although the correlation with [6] is fairly good, the correlation with [3] is quite poor. Even though the results for $\zeta = 0°$ agree very well with [3], all other results drastically differ. Differences seem to be both quantitative and qualitative. The qualitative differences are especially apparent since Cases II and IV are said to exhibit a flap divergence for $C_T/\sigma = 0.10$ in [3]. This divergence, however, did *not* appear when generating the current results. Although Case II did noticeably deform in a nose-up manner, this deformation remained statically stable for the entire C_T/σ range plotted. This "divergence" is believed to have been caused by a divergence of the trim algorithm of [3] (as supported by [16]). The quantitative differences between the codes is most severe for Cases III and IV. In these cases, [3] predicts a very large variation in damping with ply angle. This large variation, however, does not seem likely since only the inner one-eighth of the wall thickness was used to obtain the extension-twist coupling.

3.3. Numerical Issues

During the validation of the current computer code, it was found that there were three situations for which the numerical behavior of the solution became unacceptable. All three situations
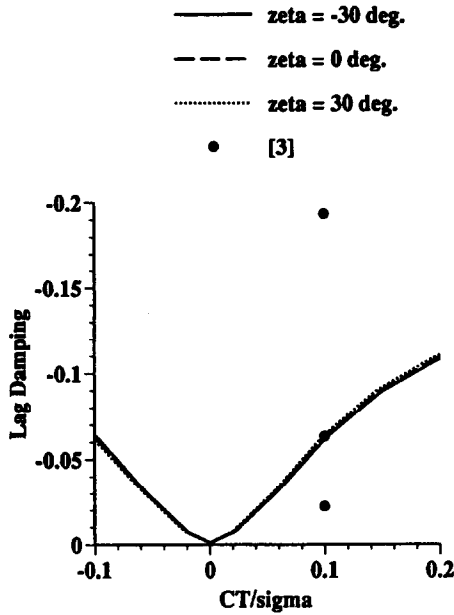
Figure 7. Lag damping for box HC III (extension-twist coupling).
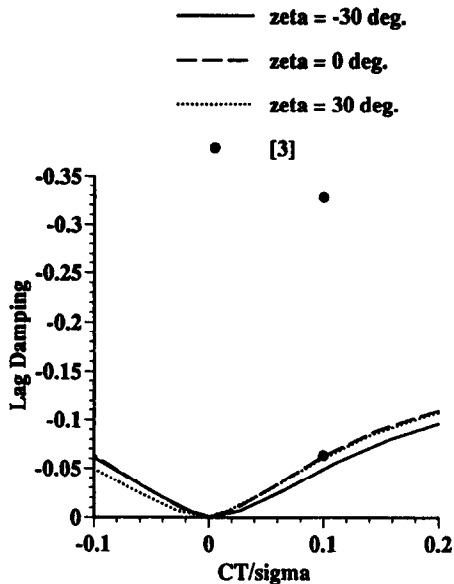

Figure 8. Lag damping for box HC IV (extension-twist coupling).

appeared only for certain ranges of physical parameters and were typically overcome by coding modifications.

First, it was found that the mixed finite element formulation yields a numerically stable set of equations only when the length of an element is smaller than some critical length.[1] In other words, if an element is too long the formulation can blow up. In all realistic cases studied, however, this critical length was longer than the blade length, meaning that even a one-element model was numerically stable.

The second case occurred for certain situations during the Newton-Raphson iterations for the equilibrium solution. In general, results were generated by allowing the program to iterate beyond convergence. Some cases, however, would eventually develop a poorly conditioned Jacobian if allowed to iterate too many cycles beyond convergence. In practice, this was not found to be

---

[1] For an isotropic beam, for example, the critical element length is proportional to $\left((EI)/(\rho\omega_{a3}^2)\right)^{1/4}$.

a problem since the divergence never occurred until after a well-converged solution had been obtained.

The third case appeared for a certain range of root pitch angles for a rotating rotor. In this case, the equilibrium solution remained unaffected, but the eigensolution was found to be incorrect. More specifically, the solution did not converge to the "exact solution" as the number of elements was increased. It was discovered that this problem occurred for cases which had eigensolutions which were sensitive to small changes in the eigenproblem matrix. Changing the code from single precision to double precision (on an IEEE computer) was found to provide the accuracy needed to obtain accurate solutions in the sensitive region. This improvement in accuracy is demonstrated by Figure 9, which is a plot of the lag damping versus thrust level for rotor R1 L3e. The solid line is a double precision result with $N = 16$. The dotted and short dashed lines are single precisions results for $N = 16$ and $N = 32$, respectively.
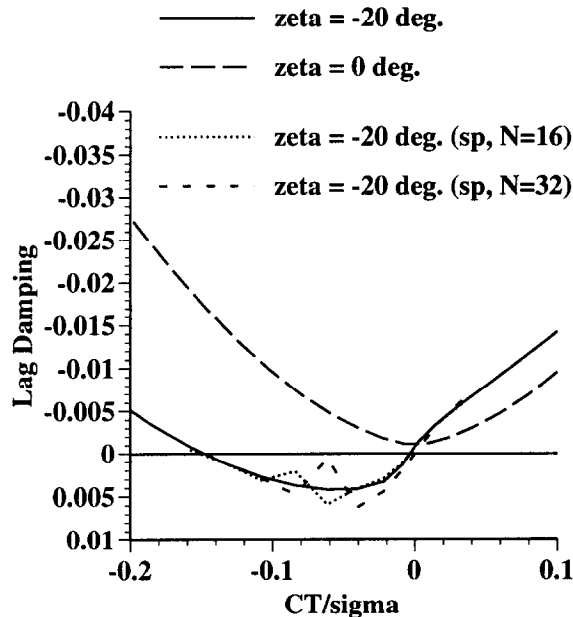

Figure 9. Plot of the eigenproblem solution's sensitivity to machine precision for a certain range of operating conditions for R1 L3e.

4. PARAMETRIC STUDIES

This section contains parametric studies of Rotors R2 and R1. Results include frequencies, dampings, and strains. Investigations of the importance of various modeling parameters are made for these extension-twist coupled rotors.

For R2, which has a lay-up of $[-20°, 70°, -20°, 70°_2, -20°]$, the nondimensional fundamental frequencies (*in vacuo*) are 0.76, 1.06, and 3.21 for lead-lag, flap, and torsion, respectively. Here and throughout this section, a positive fiber angle, ζ, is one which causes a unidirectional lay-up to have positive extension-twist coupling; this positive coupling causes the beam to develop a negative (nose-down) twist in response to a resultant tensile load acting on the beam. In addition, all frequencies and dampings plotted in this section have been normalized by the rotor speed.

Figure 10 gives the frequencies of the first four modes of this rotor. Note that the first two modes, lead-lag and flap, are highly coupled. Although this coupling promises to generate interesting behaviors, the fact that the lightly damped lead-lag mode crosses the once-per-rev line indicates that something potentially dangerous is occurring.

Figure 11 shows the predicted magnitudes of the lead-lag and the flap dampings with and without bending-shear coupling. A look at this figure shows that the coupled lead-lag and flap

modes do in fact prove interesting. The dampings indicate that the flap mode is sacrificing some of its damping for the lead-lag mode. This exchange, in fact, produces a relatively large lead-lag damping at the once-per-rev frequency crossover. In addition, the figure shows that bending-shear coupling can be important for the accurate prediction of damping.
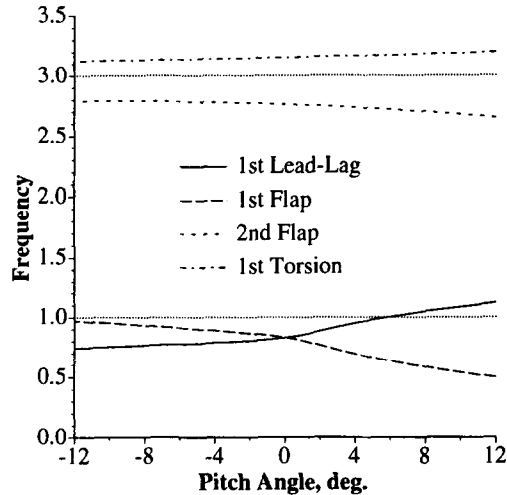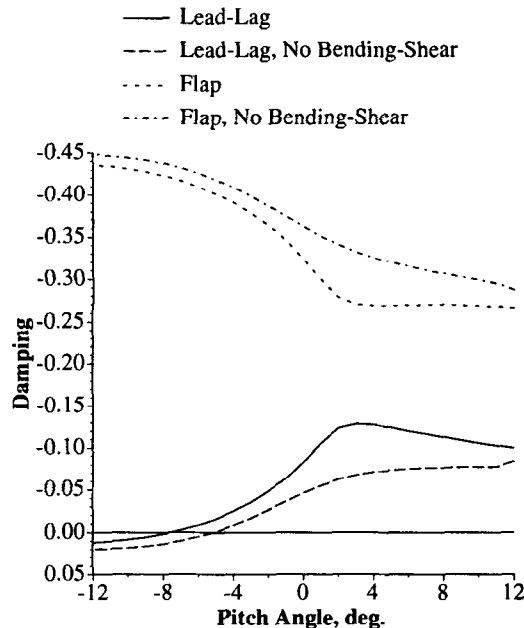
Figure 10. Normalized frequencies for rotor R2.

Figure 11. Normalized damping for rotor R2, with and without bending-shear coupling.

In conclusion, this rotor displays interesting, complex behavior which is only captured when the effects of bending-shear coupling is included in the analysis. This rotor, however, is spinning at a very high speed relative to the experimental rotor of similar dimensions described in [14]. An obvious issue, then, is whether or not this rotor will fail under the given operating conditions. Examination of the displacements shows that the maximum vertical tip displacement is approximately 30% of the blade length. Moreover, the strain levels at the root are quite high. In fact, the maximum axial strain experienced by this rotor is approximately twice the allowable for this

material, even when compared to the maximum strain allowed in the fiber direction. For this reason, this rotor is not considered to be realistic for the given operating conditions.

For each laminate of R1, plots are shown for the nondimensional lead-lag damping as a function of the blade's root pitch angle, where a positive pitch angle leads to positive lift for a rigid blade. Each plot includes results obtained for multiple values of ζ. Although ATWCS [17] was used for calculating the stiffnesses of L2e and L3e, the analysis of [18] was used to calculate the nonlinear torsional stiffness coefficient.

Figure 12 gives the lead-lag damping for laminate L2e. When looking at this figure, one of the most obvious realizations is that the cases with extension-twist coupling (i.e., $0° < \zeta < 90°$) are different from the orthotropic cases in that the coupled cases are not symmetric about zero pitch angle. The basic factor which generates this behavior is the new equilibrium position caused by the coupling.
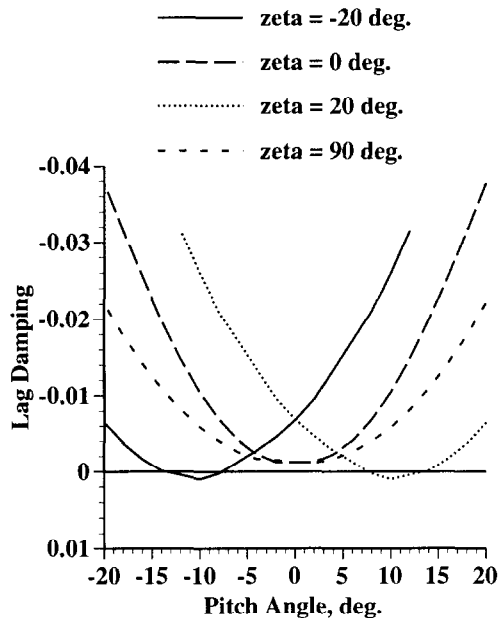

Figure 12. Normalized lag damping for $[0_2/\zeta_4]$ box beam (L2e) for rotor R1 with various values of ζ.

When extension-twist coupling is present, the centrifugally produced extension of the blade generates twist. This twist, a term due to the constitutive properties of the cross-section, changes sign when ζ changes sign. This sign change explains the drastic difference seen between the result for $\zeta = -20°$ and $\zeta = 20°$. Each of these two results, however, are simply a shift of the basic uncoupled response to the left (as for $\zeta = -20°$) or to the right (as for $\zeta = 20°$).

For example, consider the $\zeta = -20°$ curve. For this case, the extension-twist coupling causes the blade to develop positive twist (nose-up) in response to the centrifugal load. This twist causes the geometric angle of attack to be greater than that obtained without this coupling, so that at a root pitch angle of $0°$, for example, the outboard sections of the blade are actually at larger, positive pitch angles.

Unfortunately, however, this insight is very possibly one of the few significant facts discernible from this type of a plot. This conclusion is based upon the fact that comparing the damping for two different material configurations operating at the same root pitch angle is not completely valid—the large variation in torsional deformation can lead to noticeably different thrust conditions from one case to the next.

Figure 13 is similar to Figure 12 except that this new plot is for laminate L3e. As can be seen, the larger extension-twist coupling available from L3e permits a larger variation in the lag

damping with pitch angle. In addition, the zero damping cross-over is moved outside of the range of pitch angles plotted. With regards to the large damping obtained for $\zeta = -20°$, note that this level of damping might not actually be obtainable since it is associated with angles of attack of approximately 11° and 16° at midspan and near the blade's tip, respectively.
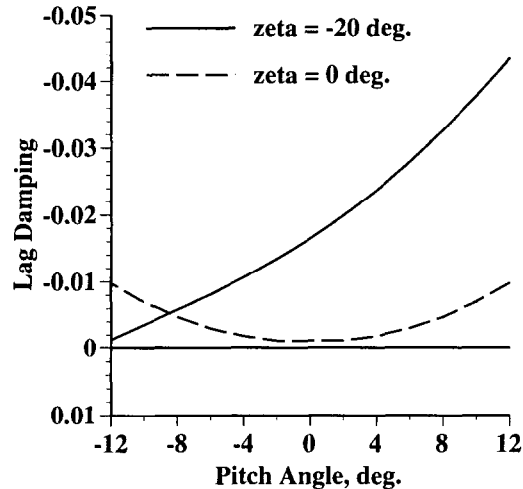

Figure 13. Normalized lag damping for $[\zeta, \zeta - 90, \zeta, (\zeta - 90)_2, \zeta]$ box beam (L3e) for rotor R1 with two values of ζ.

In addition, caution should be used before accepting these designs as structurally sound from a materials failure perspective. Initial maximum strain failure analysis has indicated that the $\zeta = 90°$ case in Figure 12 has failed at a pitch angle of 12° if dynamic loads are approximated as increasing the equilibrium strain levels by a factor of 1.5. Additional preliminary failure checks indicate that these structures tend to be near failure for these operating conditions, but additional checks will need to be made in order to better understand how close the structures are to failure.

Next, consider plotting the lag damping of L3e versus a nondimensionalized thrust. Figure 14 shows that plotting versus C_T/σ (coefficient of thrust/rotor solidity) is indeed better for judging the damping variation at a given thrust condition due to ply angle changes. This new plot demonstrates that there is less of an advantage to using the coupled configuration for positive thrust conditions than is implied by Figure 13. In fact, Figure 14 indicates that the damping for the coupled configuration becomes small for a slightly negative thrust level, with the configuration eventually becoming unstable for sufficiently large negative thrust.

Figure 14 also includes results which used TAIL stiffnesses as input (in addition to ATWCS stiffnesses), where both the full 6×6 TAIL stiffness matrix was used and an approximate 6×6 stiffness matrix which neglected the bending-shear coupling. Figure 14 indicates that results based on the 4×4 stiffness matrix ATWCS agree well with those based on TAIL for this configuration. In addition, it shows that the omission of bending-shear coupling causes little error for this case. Figure 15 is similar to Figure 14 except that the laminate is now L2e ($[0_2/\zeta_4]$) instead of L3e ($[\zeta, \zeta - 90, \zeta, (\zeta - 90)_2, \zeta]$). Note the severity of the instability is decreased, but the stable regime exhibits essentially the same margin of stability as the unidirectional blade.

Now, consider the effect of 2.5° of precone for R1 L3e ($[\zeta, \zeta - 90, \zeta, (\zeta - 90)_2, \zeta]$). Figure 16 shows that this amount of precone has a negligible effect on the lag damping for this configuration. Figures 17 and 18 show the effect that this precone level has on the beam's extensional strain and the flapwise bending curvature for $C_T/\sigma = 0.21$ and a ply angle $\zeta = -20°$. The extensional strain, which is dominated by centrifugal force, is practically unaffected by this small precone angle. The flapwise curvature, however, is noticeably reduced at the root by the precone. This reduction is as expected and contributes towards lowering the large axial strain levels on the bottom of the
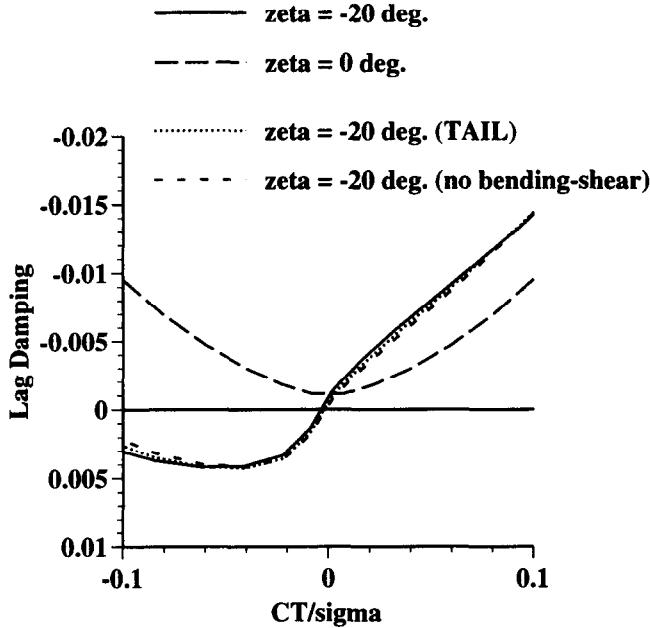
Figure 14. Normalized lag damping for $[\zeta, \zeta - 90, \zeta, (\zeta - 90)_2, \zeta]$ box beam (L3e) for rotor R1 for two values of ζ.
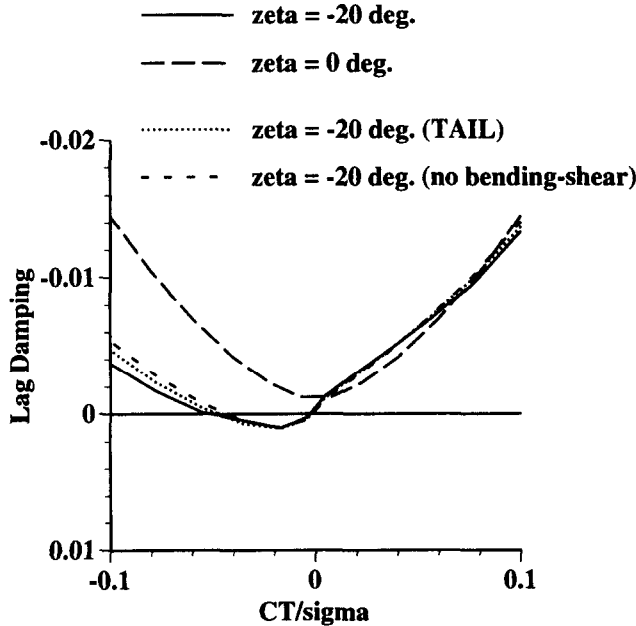

Figure 15. Normalized lag damping for $[0_2/\zeta_4]$ box beam (L2e) for rotor R1 with various values of ζ.

box beam. Note that γ_{11} and κ_2 are unknowns in the present analysis and therefore calculated directly by the current code without the need of differentiating displacement variables.

5. DISCUSSION, CONCLUDING REMARKS, AND RECOMMENDATIONS

In Part I of this two-part paper, an aeroelastic stability analysis was presented for isolated hingeless, composite rotor blades in the hovering flight condition, which was based on a geo-
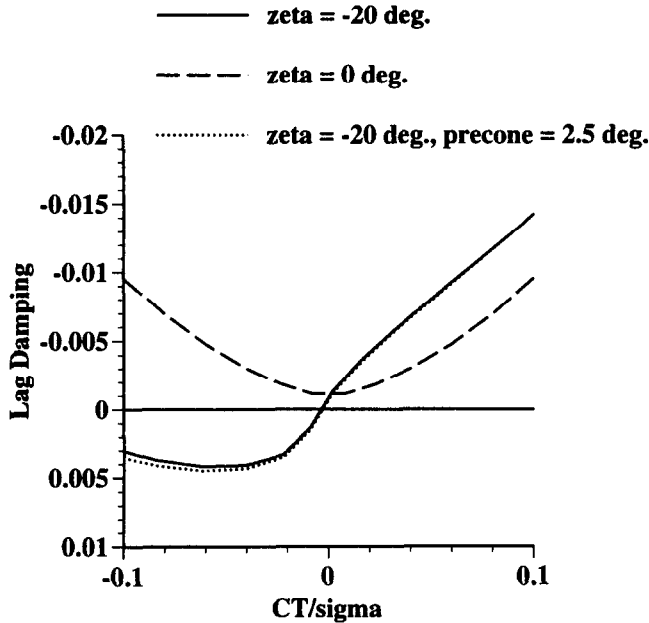
Figure 16. Variation in lag damping with the addition of 2.5° of precone for config-uration R1 L3e ($[\zeta,\zeta - 90,\ \zeta,(\zeta - 90)_2,\zeta]$).
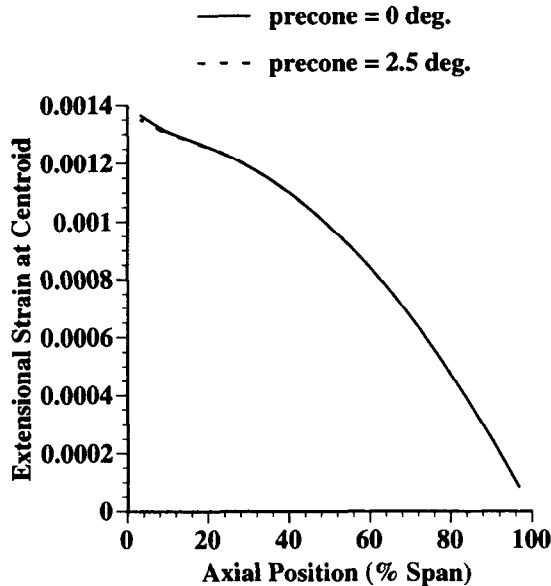

Figure 17. Plot of γ_{11} (extensional strain) for two different values of precone for $C_T/\sigma = 0.21$ for R1 L3e ($[\zeta, \zeta - 90, \zeta, (\zeta - 90)_2, \zeta]$) with $\zeta = -20°$.

metrically exact, mixed finite element method. The formulation is comprised of separate, but compatible, cross-sectional (two-dimensional) and global or beam (one-dimensional) equations.

Herein, the focus was to present numerical results obtained from this analysis. A FORTRAN program called STAB was developed based on the analysis of Part I. Through previous publica-tions and this paper, STAB was thoroughly validated against analytical and existing experimental results for equilibrium, dynamic, and stability calculations. The validations encompassed both small and large equilibrium deflections. In addition, extensive correlations were performed against experimental composite results, including both static and dynamic cases. These studies indicate that the current approach accurately represents large static deflections and linearized dynamics
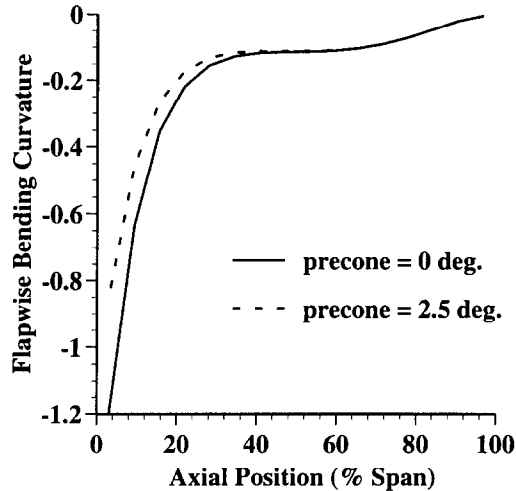
Figure 18. Plot of κ_2 (flapwise bending curvature) for two different values of precone for $C_T/\sigma = 0.21$ for R1 L3e ($[\zeta, \zeta - 90, \zeta, (\zeta - 90)_2, \zeta]$) with $\zeta = -20°$.

about equilibrium of composite beams quite well. The aeroelastic effects are only as accurate as the aerodynamic modeling.

Comparisons of current results with the lead-lag damping results from [3] illuminated large discrepancies between the two analyses but seemed to reproduce results obtained by [6] for the same cases.

The accuracy of the composite predictions, of course, depends on the quality of the cross-sectional stiffnesses. The two-dimensional cross-sectional analyses used herein, however, gave nearly identical results for many cases; this is believed to be due to their high quality. The performance of "classical" stiffnesses (which ignore all shear deformation effects), however, was poor for several cases, in agreement with [9]. Although the stability cases studied were not typically very sensitive to the nonclassical couplings, there are cases for which a significant error is exhibited when bending-shear coupling is neglected. This indicates that for general purpose analysis, one needs to include this phenomenon.

Validation studies demonstrated that the current approach, though generally quite robust, has difficulties for some groupings of physical parameters. First, the method was found to require elements to be shorter than a maximum length for numerical stability. This critical length exceeded the blade length for physically meaningful problems, so that even a one-element model was numerically stable. Second, the Newton-Raphson iterations used in obtaining the equilibrium solution were sometimes found to diverge from the solution if the algorithm was allowed to iterate for too many (i.e., unnecessary) cycles; in practice, this was not found to be a problem since the divergence never occurred until after a well-converged solution had been obtained. Third, the current method exhibited sensitivity to numerical precision in the eigensolution phase, which was overcome by using double precision (IEEE) arithmetic.

The convergence rate for this finite element stability analysis was shown to be very good. Specifically, the relative error varied inversely with N^3 for the flapwise deflection of a high-thrust case (where N is the number of elements); the relative error varied inversely with N^6 for the lead-lag modal damping of a low-thrust case.

The fact that a reduced 4×4 stiffness matrix (reduced as pointed out in [9] by minimization of the strain energy with respect to the transverse shear parameters) does a good job of representing a complete 6×6 stiffness matrix for many cases suggests that current rotor aeroelastic analyses based on "classical theory" (which completely neglects shear deformation) such as GRASP [19] can be modified to incorporate certain composite effects without having to introduce additional unknowns and equations. Any new code, however, should use a complete 6×6 matrix for

generality. In fact, an important extension to this work would be to incorporate the effects of restrained warping, which may require the stiffness matrix to be expanded beyond 6×6.

Other reasonable extensions to the present work include the addition of multiple load path capabilities (for bearingless rotors) and additional rotor configuration parameters such as initial curvature and spanwise varying cross-sections. The accommodation of manufacturing and failure issues would also provide interesting and important extensions to this work. Other new directions for this work could be found by developing an analysis for forward flight or by adding body degrees of freedom. Finally, nonlinear lifting theories and dynamic inflow effects would noticeably increase the realism of the aerodynamic modeling. In addition to extensions to the analysis, there is still plenty of room for learning more about composite stability results with the present methodology, such as through study of more realistic rotor-blade cross-sections with general-purpose numerical cross-sectional analyses.

REFERENCES

1. R.A. Ormiston, Investigations of hingeless rotor stability, *Vertica* **7** (2), 143–181 (1983).
2. E.C. Smith and I. Chopra, Aeroelastic response and blade loads of a composite rotor in forward flight, *Proceedings of the 33ʳᵈ Structures, Structural Dynamics, and Materials Conference*, Paper No. 92-2466-CP, Dallas, TX, (April 13–17, 1992).
3. C.H. Hong and I. Chopra, Aeroelastic stability analysis of a composite rotor blade, *Journal of the American Helicopter Society* **30** (2), 57–67 (1985).
4. R. Chandra and I. Chopra, Experimental-theoretical investigation of the vibration characteristics of rotating composite box-beams, Presented at the *American Helicopter Society National Technical Specialists' Meeting on Rotorcraft Dynamics*, Arlington, TX, (November 1989).
5. A.D. Stemple and S.W. Lee, Large deflection static and dynamic finite element analysis of composite beams with arbitrary cross-sectional warping, *Proceedings of the 30ᵗʰ Structures, Structural Dynamics, and Materials Conference*, Paper No. 89-1363, Mobile, AL, (April 3–5, 1989).
6. K.A. Yuan, P.P. Friedmann and C. Venkatesan, A new aeroelastic model for composite rotor blades with straight and swept tips, *Proceedings of the 33ʳᵈ Structures, Structural Dynamics, and Materials Conference*, Paper No. 92-2259-CP, Dallas, TX, (April 13–17, 1992).
7. D.H. Hodges, A mixed variational formulation based on exact intrinsic equations for dynamics of moving beams, *International Journal of Solids and Structures* **26** (11), 1253–1273 (1990).
8. D.H. Hodges, A.R. Atılgan, M.V. Fulton and L.W. Rehfield, Free-vibration analysis of composite beams, *Journal of the American Helicopter Society* **36** (3), 36–47 (1991).
9. D.H. Hodges, A.R. Atılgan, C.E.S. Cesnik and M.V. Fulton, On a simplified strain energy function for geometrically nonlinear behavior of anisotropic beams, *Composites Engineering* **2** (5–7), 513–526 (1992).
10. A.R. Atılgan, D.H. Hodges and M.V. Fulton, Nonlinear deformation of composite beams: Unification of cross-sectional and elastica analyses, *Applied Mechanics Reviews* **44** (11), Part 2, S9–S15 (1991).
11. M.V. Fulton, Stability of elastically tailored rotor blades, Ph.D. Dissertation, School of Aerospace Engineering, Georgia Institute of Technology, Atlanta, GA, (1992).
12. NASA Ames Research Center, Methodology assessment—Phase 2 continuation, ARC 275a, (February 1981).
13. R.V. Hodges, M.W. Nixon and L.W. Rehfield, Comparison of composite rotor blade models: A coupled-beam analysis and an MSC/NASTRAN finite-element model, NASA TM 89024, (1987).
14. D.L. Sharpe, An experimental investigation of the flap-lag-torsion aeroelastic stability of a small-scale hingeless helicopter rotor in hover, NASA TP 2546, (1986).
15. D.H. Hodges, Nonlinear equations of motion for cantilevered rotor blades in hover with pitch link flexibility, twist, precone, droop, sweep, torque offset, and blade root offset, NASA TM X-73,112, (1976).
16. I. Chopra, Private communication, (July 14, 1992).
17. V.L. Berdichevsky, E.A. Armanios and A. Badir, Theory of anisotropic thin-walled closed-cross-section beams, *Composites Engineering* **2** (5–7), 411–432 (1992).
18. L.W. Rehfield, Design analysis methodology for composite rotor blades, Presented at the 7ᵗʰ *DoD/NASA Conference on Fibrous Composites in Structural Design*, Paper No. AFWAL-TR-85-3094, pp. (V(a)-1)–(V(a)-15), Denver, CO, (June 17–20, 1985).
19. D.H. Hodges, A.S. Hopkins and D.L. Kunz, Analysis of structures with rotating, flexible substructures applied to rotorcraft aeroelasticity, *AIAA Journal* **27** (2), 192–200 (1989).